

Article

Chemical State of Potassium on the Surface of Iron Oxides: Effects of Potassium Precursor Concentration and Calcination Temperature

Md. Ariful Hoque ¹, Marcelo I. Guzman ^{1,*} , John P. Selegue ¹  and Muthu Kumaran Gnanamani ²¹ Department of Chemistry, University of Kentucky, Lexington, KY 40506, USA² Center for Applied Energy Research, University of Kentucky, Lexington, KY 40511, USA

* Correspondence: marcelo.guzman@uky.edu; Tel.: +1-(859)-3232892

Abstract: Potassium is used extensively as a promoter with iron catalysts in Fisher–Tropsch synthesis, water–gas shift reactions, steam reforming, and alcohol synthesis. In this paper, the identification of potassium chemical states on the surface of iron catalysts is studied to improve our understanding of the catalytic system. Herein, potassium-doped iron oxide (α -Fe₂O₃) nanomaterials are synthesized under variable calcination temperatures (400–800 °C) using an incipient wetness impregnation method. The synthesis also varies the content of potassium nitrate deposited on superfine iron oxide with a diameter of 3 nm (Nanocat[®]) to reach atomic ratios of 100 Fe:x K ($x = 0$ –5). The structure, composition, and properties of the synthesized materials are investigated by X-ray diffraction, differential scanning calorimetry, thermogravimetric analysis, Fourier-transform infrared, Raman spectroscopy, inductively coupled plasma-atomic emission spectroscopy, and X-ray photoelectron spectroscopy, as well as transmission electron microscopy, with energy-dispersive X-ray spectroscopy and selected area electron diffraction. The hematite phase of iron oxide retains its structure up to 700 °C without forming any new mixed phase. For compositions as high as 100 Fe:5 K, potassium nitrate remains stable up to 400 °C, but at 500 °C, it starts to decompose into nitrites and, at only 800 °C, it completely decomposes to potassium oxide (K₂O) and a mixed phase, K₂Fe₂₂O₃₄. The doping of potassium nitrate on the surface of α -Fe₂O₃ provides a new material with potential applications in Fisher–Tropsch catalysis, photocatalysis, and photoelectrochemical processes.

Keywords: hematite; potassium; Fisher–Tropsch; photocatalysis

Citation: Hoque, M.A.; Guzman, M.I.; Selegue, J.P.; Gnanamani, M.K. Chemical State of Potassium on the Surface of Iron Oxides: Effects of Potassium Precursor Concentration and Calcination Temperature. *Materials* **2022**, *15*, 7378. <https://doi.org/10.3390/ma15207378>

Academic Editor: Stefano Agnoli

Received: 14 September 2022

Accepted: 19 October 2022

Published: 21 October 2022

Publisher's Note: MDPI stays neutral with regard to jurisdictional claims in published maps and institutional affiliations.



Copyright: © 2022 by the authors. Licensee MDPI, Basel, Switzerland. This article is an open access article distributed under the terms and conditions of the Creative Commons Attribution (CC BY) license (<https://creativecommons.org/licenses/by/4.0/>).

1. Introduction

Potassium has been used widely as a promoter for iron catalysts in Fisher–Tropsch synthesis, whereby syngas (CO + H₂) is converted into liquid fuels [1–4]. As a promoter with iron catalysts, potassium increases CO chemisorption, but strongly inhibits hydrogen chemisorption in comparison to bare iron oxide [5,6]. Potassium donates electrons to adjacent iron centers that help to strengthen the Fe–C bonds while weakening the Fe–H bonds, increasing the adsorption of CO and decreasing the adsorption of H₂, respectively [7,8]. This potassium-iron interaction and the superiority of potassium to other alkali or alkali earth metal promoters have been found to be advantageous in Fisher–Tropsch synthesis [9–13]. In addition, potassium is also used as a promoter with other catalysts (e.g., cobalt-based, aluminum-based, copper-based, manganese-based, etc.) for Fisher–Tropsch synthesis, hydrodesulfurization, steam reforming, methane (CH₄) reforming, alcohol synthesis, alkene synthesis, water–gas-shift reactions, nitric oxide (NO_x) removal, ammonia (NH₃) synthesis, oxidation, etc. [10,12,14–19].

For the processes mentioned above, the incipient wetness impregnation method (IWIM) is often used to create catalysts by doping their surfaces with potassium. Potassium hydroxide (KOH) [16], or potassium salts of carbonate [11], bicarbonate [20], nitrate [21], and acetate [22], have been used to prepare potassium-doped catalysts by IWIM.

Although a few different calcination temperatures at low potassium loadings have been explored [9,14,19], there has been no systematic study varying simultaneously both the potassium content and the temperature of calcination to generate the catalysts of interest. For example, the calcination of KOH with aluminum-magnesium catalysts at 400 °C has been used in the hydrodesulfurization of dibenzothiophene [16]. Similarly, for Fisher–Tropsch synthesis, potassium oxide (K₂O) has been generated during the calcination (350–500 °C) of potassium carbonate (K₂CO₃) on iron [16], iron-manganese [9], iron-cobalt [19], and reduced graphene oxide-supported iron catalysts [18]. This K₂CO₃ precursor has also served to produce K₂O on zinc-chromium-based catalysts, calcined at 400 °C, which are used for the synthesis of isobutanol [17]. Alternatively, the potassium hydrogen carbonate (KHCO₃) precursor has been used on iron and iron-manganese catalysts, calcined at 300 °C, to create K₂O for Fisher–Tropsch synthesis [20].

Interestingly, potassium nitrate (KNO₃) has been calcined with gold-titanium-silicate [23] and cobalt-copper-titanate [24] at ≤350 °C with the objective of creating catalysts for converting carbon dioxide (CO₂) into propanol and long-chain hydrocarbons, respectively. For applications in Fisher–Tropsch synthesis, KNO₃ has been calcined in the range of 300–500 °C with iron-based catalysts [13,21,25]. Furthermore, in order to decompose NO₂, the in situ generation of the K₂O promoter was attempted over copper catalysts from KNO₃, calcined at 400 °C [14]. However, the use of low loadings of KNO₃ precursor to dope catalysts with small concentrations of K₂O has been assumed to proceed at specific calcination temperatures, although typical instrumental limitations may have prevented the verification of the chemical and electronic states of interest.

An additional, almost unnoticed problem associated with calcination when it is used to create catalysts with low loadings of the potassium precursor is that the decomposition behavior of the precursor (e.g., KNO₃) can change with increasing temperature. For example, at each temperature increment, the decomposition products that are generated can vary significantly, affecting the catalytic behavior of the material. Therefore, in this work, we perform a systematic study to optimize the calcination temperature of KNO₃ (as the only precursor) on superfine iron oxide with a diameter of 3 nm (Nanocat[®]) and monitor the decomposition products. The surface-loaded potassium–iron oxides are synthesized by IWIM, with atomic ratios of 100 Fe:*x* K (*x* = 0, $\frac{1}{2}$, 1, 2, 3, and 5). In other words, we study the chemical and electronic states generated from variable amounts of KNO₃ precursor with a fixed iron content. The most highly potassium-doped sample, 100 Fe:5 K, was selected to characterize its calcination in air from 400 °C to 800 °C, to understand how the decomposition proceeds.

This work studies the effects of both potassium loading and calcination temperature on the structure and electronic state of synthesized potassium-doped iron oxide. Based on recent studies, the calcination temperature may affect the catalytic activity of iron oxide-based catalysts by changing the electronic and chemical state of potassium in the vicinity of iron oxide [26–28]. On the other hand, the changing composition of potassium may also affect active sites on the catalyst and, thereby, the catalytic performance [29–31]. An iron-based catalyst was synthesized using a potassium nitrate precursor with varying potassium loading and a calcination temperature of 400 or 500 °C to study the CO₂ hydrogenation reaction [32–34]. The effect of potassium loading for the selective catalytic reduction of NO_x with an iron-based catalyst has been investigated [35]. Potassium promotion on iron catalysts obtained by pyrolysis has been explored for the purpose of ammonia synthesis [36]. However, and to the best of our knowledge, there is no systematic work available in the literature that has varied the calcination temperature of potassium-loaded iron oxide and simultaneously studied the electronic and structural properties of both components.

Overall, evaluating the influence of the promoter effects (e.g., metal salts [37]) in the environment of iron oxides can be a challenging experimental task, due to the large number of variables that need to be controlled during the synthesis (e.g., temperature, pressure, amount of promoter precursor, etc.). Simultaneously, there is a need to characterize low levels of the promoter and its structural and electronic properties [34,37–39]. Even small

changes in the iron oxide phase, composition, and morphology (e.g., by the addition of structural (Al_2O_3) or electronic (K_2O) promoters [34,38,39]) can affect the catalysts' performance and the mechanism of catalysis for important processes such as the synthesis of ammonia and the Fisher–Tropsch process [38,39]. Therefore, to reach a better understanding of the catalytic performance and catalysis mechanism of potassium (promoter)-based iron oxide catalysts, it is important to know in detail the electronic state and structural parameters of both the promoter and catalyst reported in this work.

2. Materials and Methods

2.1. Preparation of Potassium-Doped Iron Oxides

Nanocat[®] superfine iron oxide (Mach I Inc., King of Prussia, PA, USA, 99.3%) of hematite phase ($\alpha\text{-Fe}_2\text{O}_3$) was dried at 110 °C for 3 h in an oven (Blue M, Single-Wall Transite Oven, White Deer, PA, USA). The raw material has a Brunauer–Emmett–Teller (BET) surface area of 244.24 m² g⁻¹, a particle size of 3 nm, and a bulk density of 0.05 g cm⁻³. For the potassium precursor, KNO_3 was obtained commercially (Sigma-Aldrich, St. Louis, MO, USA, 99.0%). Both Nanocat[®] and KNO_3 were used to obtain a series of $\alpha\text{-Fe}_2\text{O}_3$ materials loaded with potassium, following the IWIM. For the syntheses, 15.0 mL solutions of KNO_3 were prepared in deionized water at concentrations of 0.0213, 0.0426, 0.0852, 0.1277, and 0.2130 M. Each solution was added slowly to 5.0 g of $\alpha\text{-Fe}_2\text{O}_3$ placed in a rotating 250.0 mL round bottom flask using a customized West-type condenser provided with a polytetrafluoroethylene stopcock for dropwise addition. Rotation of the flask at a rate of 20 rpm was provided with a rotavapor (Brinkmann, Wood Dale, IL, USA, R110). The resulting materials were dried at 110 °C overnight in porcelain crucibles. These dried samples were then calcined in a muffle furnace (Thermo Scientific, Waltham, MA, USA, Lindberg) at 400 °C for 5 h in air. By varying the amount of KNO_3 loaded, materials with atomic ratio 100 Fe:x K ($x = 0, \frac{1}{2}, 1, 2, 3, \text{ and } 5$) were obtained. In addition, the 100 Fe:5 K material was further calcined in air for 5 h at 500 °C, 600 °C, 700 °C, and 800 °C.

2.2. Characterization of Materials

Samples of 0.2500 g were weighed accurately into a Teflon MARSXpress vessel and 10.0 mL of nitric acid (HNO_3 , Acros Organics, Morris Plane, NJ, USA, ACS reagent, 65%) was added. The vessels were then closed and placed into a microwave digestion system (One-Touch Technology, Matthews, NC, USA, Mars 6), where the digestion was carried out with a power of 1.3 kW using a temperature ramp reaching 200 °C in 25 min, which was held at 200 °C for an extra 10 min. The digested samples were then allowed to cool for at least 3 h before opening the vessels. After cooling, the digested sample was augmented to a final volume of 10.0 mL with 10% nitric acid, from which 1.0 mL aliquots were diluted 10 times with 10% nitric acid to prepare stock solutions for potassium analysis. A further 1000-times dilution of the stock solution in 10% HNO_3 was used for the iron analysis.

The analysis of potassium and iron in the previous samples was performed by inductively coupled plasma optical emission spectroscopy (ICP-OES, Varian, Santa Clara, CA, USA, Vista-PRO CCD Simultaneous). The analysis for iron considers an average for emission maxima at 234.35, 238.20, 239.56, and 259.94 nm, while for potassium, the maximum at 766.49 nm is used. Multi-elemental standards of iron and potassium (Ultra Scientific, Santa Clara, CA, USA, with each analyte at 1000 $\mu\text{g mL}^{-1}$) were used to create calibration curves with solutions of concentration at $\frac{1}{2}$, 1, 5, 10, and 50 ppm in 10% HNO_3 . Five parts per million (ppm) standards were used as check standards, and 1 ppm yttrium in 10% HNO_3 served as an internal standard (CPI International, 1000 $\mu\text{g mL}^{-1}$ in 2% HNO_3). Samples were analyzed in triplicate. The operating conditions of the ICP-OES instrument were as follows: 1.20 kW radio-frequency power, 15.0 L min⁻¹ plasma flow rate, 1.50 L min⁻¹ auxiliary flow rate, 3 mL min⁻¹ sample uptake, 35 s read delay, and 0.9 L min⁻¹ nebulizer gas flow rate.

The X-ray diffraction (XRD) patterns of the samples were obtained with B8 Advance Bruker AXS diffractometer with Cu K α incident radiation ($\lambda = 0.15418$ nm). XRD data

were recorded from 10° to 90° , at a scan rate of 1° min^{-1} . Thin films of the materials were created by finely grinding the solids in an agate mortar, suspending the powders in water, depositing the suspensions on glass slides, and air-drying. The diffraction pattern of an empty sample holder was recorded and subtracted during the data processing.

A TA Instruments Q5000 was used for the thermogravimetric analysis (TGA) of samples heated under a nitrogen atmosphere, at a flow rate of 25 mL min^{-1} and a heating rate of $10^\circ \text{ C min}^{-1}$ from 30 to 800° C .

The X-ray photoelectron spectroscopy (XPS) surface analysis was recorded with a pass energy of 50 eV at a step size of 0.1 eV and X-ray beam size of $400 \mu\text{m}$, using a Thermo Scientific spectrometer (K-Alpha) with an Al $K\alpha$ anode (1486.6 eV photon energy, 300 W) excitation source.

The Raman spectra (200 scans) were recorded using a DXR Raman microscope (Thermo Scientific). a diode-pumped Nd:YVO₄ laser was used as the excitation source (532 nm), with 2 mW power and a $50 \mu\text{m}$ aperture slit for Raman characterization.

Transmission electron microscopy (TEM) analysis was carried out using a Talos F200X instrument (Thermo Scientific) operated at an acceleration voltage of 200 kV . Images were recorded with Ceta 16M camera and Velox software (FEI). Selected-area electron diffraction patterns (SAED) and energy-dispersive X-ray spectroscopy (EDS) with four silicon drift detectors were also investigated from the electron micrographs. Before analysis, the as-prepared particles were dried in an oven for 24 h at 120° C . The dry particles were then suspended in ethanol and sonicated for 30 min prior to being dropped onto a TEM grid with a lacy support film, which was allowed to air-dry for about 6 h .

3. Results and Discussion

3.1. Powder X-ray Diffraction Analysis

Figure 1 shows the XRD patterns of bare $\alpha\text{-Fe}_2\text{O}_3$ and the materials doped with increasing potassium content under a calcination temperature of 400° C . The diffraction peaks of bare $\alpha\text{-Fe}_2\text{O}_3$ (100 Fe:0 K) centered at 24.2° , 33.1° , 35.6° , 54.1° , 62.5° , and 63.8° are labeled, respectively, as (012), (104), (110), (116), (214), and (300) on the reflections at the bottom of Figure 1, which reveal the crystalline phase of hematite. The low crystallinity of the undoped nanomaterial explains the low intensity and large peak broadening observed. The intensity of the previous reflections becomes larger for the K-doped materials with better-defined diffraction peaks in Figure 1, reflecting increased crystallinity. Moreover, all the peaks in the doped material are perfectly indexed as iron oxide with a hematite phase, with the rhombohedral lattice system (hexagonal axes, space group R3c), and with JCPDS card number #033-0664. The potassium-doped materials show the main characteristic peaks of $\alpha\text{-Fe}_2\text{O}_3$ at 2θ values of 24.2° , 33.1° , 35.6° , 40.8° , 49.5° , 54.1° , 62.5° , 63.8° , 69.8° , 72.1° , 75.6° , 77.9° , 80.9° , 83.2° , 85.2° , and 88.7° , corresponding to diffraction from the planes (012), (104), (110), (113), (024), (116), (112), (214), (300), (208), (1010), (217), (036), (128), (0210), (134), and (226).

Figure 1 does not display any typical diffraction peaks of either KNO_3 or KNO_2 , either because these species are well-dispersed over the surface and pores of $\alpha\text{-Fe}_2\text{O}_3$ without forming detectable aggregates, or because very low concentrations of these species remain after IWIM. Similarly, the negative detection of K_2O or any other mixed oxide phase(s) (Figure 1), even for the largest potassium loading (5 K), may be due to the stability of KNO_3 at 400° C . The previous hypotheses are verified below for the XRD patterns of 100 Fe:5 K material in Figure 2 (calcined at higher temperatures than in Figure 1), and by additional thermal spectroscopic analyses, which will be discussed later. No new diffraction peaks from hematite are observed upon increasing the calcination temperature from 400 to 700° C (Figure 2), in agreement with the JCPDS card #033-0664. However, the calcination at 800° C in Figure 2 shows peaks marked as (1) black asterisks for the cubic phase of K_2O (JCPDS #027-0431) and (2) red crosses for the hexagonal phase of $\text{K}_2\text{Fe}_{22}\text{O}_{34}$ (JCPDS #031-1034), respectively. a close-up of the top panel of Figure 2 at 800° C is displayed in Figure S1 (Supplementary Materials) with the corresponding position shown for the reflections of K_2O and $\text{K}_2\text{Fe}_{22}\text{O}_{34}$.

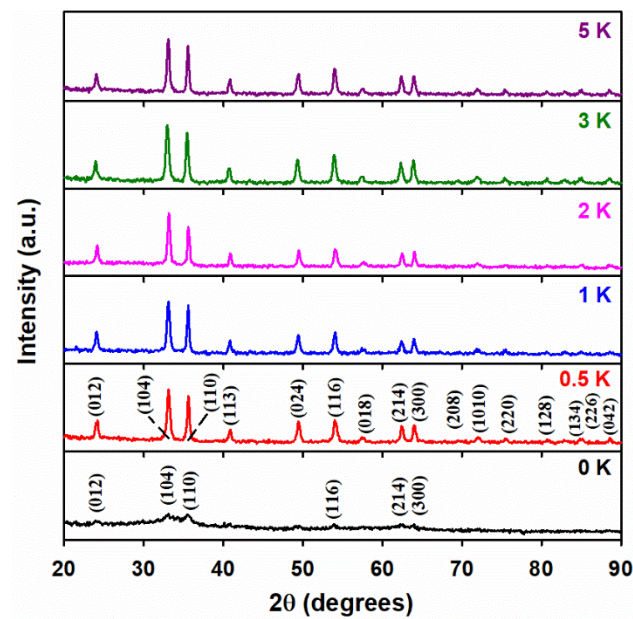


Figure 1. X-ray diffraction (XRD) patterns of 100 Fe: x K materials, with the atomic ratio of potassium (x) indicated in each panel. The assigned Miller indices match the hematite phase of iron oxide.

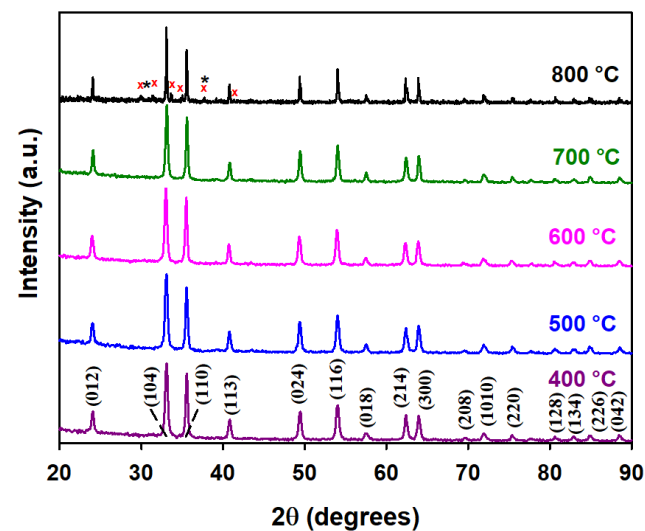


Figure 2. XRD patterns of the 100 Fe:5 K material calcined at the temperature indicated in each panel. The assigned Miller indices match the hematite phase of iron oxide. The peaks are marked as black asterisks (*) for K_2O and as red crosses (x) for $K_2Fe_{22}O_{34}$.

Potassium nitrate (KNO_3) and its decomposition products, potassium nitrite (KNO_2), and potassium superoxides, (KO_2 , JCPDS #010-0235) were not observed in Figure 2. K_2O can also absorb water and form potassium hydroxide [40]. The in situ formation of potassium hydroxide (KOH) can also be ruled out by the comparison with JCPDS #015-0890. Therefore, the XRD pattern at 800 °C confirms the presence of hematite, potassium oxide, and potassium–iron mixed oxide. The relative compositions of these three species are calculated to be 82.68%, 1.83%, and 15.49%, respectively, using the semiquantitative peak area integration in Figure 2. The XRD patterns in Figure 2 become sharper with increasing calcination temperature, reflecting their increased crystallinity.

The effects of KNO₃ loading and calcination temperature on the average crystallite size (D) of the K-doped α -Fe₂O₃ can be interpreted by applying Scherrer's equation:

$$D = \frac{k \lambda}{\beta \cos(\theta)}, \quad (1)$$

to the major diffraction peak corresponding to the (104) plane, where $k = 0.9$ is the shape factor, $\lambda = 0.15418$ nm is the X-ray wavelength, β is the full width at half-maximum for the (104) reflection in radians, and θ is the Bragg angle. Table 1 displays how the crystallite sizes of the iron oxides vary with doping and calcination. Indeed, the crystallite size increases significantly with a small addition of potassium. For example, the 4.2 nm crystallite size of undoped α -Fe₂O₃ (100 Fe:0 K) increases to 16.1 nm for the 100 Fe: $\frac{1}{2}$ K material. For the further addition of potassium, the crystallite size remains almost the same at a constant calcination temperature of 400 °C. However, increasing calcination temperature leads to significant growth, up to a maximum of 36.6 nm at 800 °C.

Table 1. Crystallite size (D) and lattice parameters (a and b) for variable potassium loading (x) and calcination temperature (T).

x ⁱ	T (°C)	D (nm) ⁱⁱ	a (Å) ⁱⁱⁱ	c (Å) ⁱⁱⁱ
0	400	4.15	5.059	13.746
$\frac{1}{2}$	400	16.1	5.042	13.782
1	400	18.1	5.047	13.787
2	400	19.3	5.040	13.761
3	400	17.1	5.063	13.844
5	400	20.0	5.044	13.794
5	500	20.0	5.051	13.807
5	600	21.2	5.058	13.829
5	700	23.6	5.046	13.780
5	800	36.6	5.067	13.841

ⁱ Atomic ratio of potassium for 100 Fe: x K ($0 \leq x \leq 5$), ⁱⁱ from Scherrer's equation, ⁱⁱⁱ from the interplanar spacing and Bragg's law.

The lattice parameters of the materials reported in Table 1 are calculated using equations that relate to the interplanar spacing, d_{hkl} (Equation (2), for the Miller indices, hkl) [41], with Bragg's law (Equation (3)):

$$\frac{1}{d_{hkl}^2} = \frac{4}{3} \times \left(\frac{h^2 + hk + l^2}{a^2} \right) + \frac{l^2}{c^2}, \quad (2)$$

$$2d_{hkl} \sin(\theta) = n \lambda, \quad (3)$$

where n is a positive integer and λ is the incident wavelength. Solving the equations for d_{110} and d_{104} for the planes (110) and (104) produces the lattice parameters of $a = b$, and c , which are reported in Table 1. Indeed, there is no significant change in the values of the lattice parameters a and c for undoped and K-doped α -Fe₂O₃ materials, calcined at different temperatures (Table 1).

Therefore, the crystallographic structure of hematite is largely preserved under the potassium loadings and calcination temperatures explored, indicating that potassium is not incorporated into the bulk defects of the α -Fe₂O₃ lattice. This is also evident from the larger cation size of K⁺ (138 pm) than Fe³⁺ (65 pm) [42]. Instead, the large K⁺ ions form K₂O and a mixed phase of K-Fe oxides, K₂Fe₂₂O₃₄.

3.2. Thermal Analysis

The TGA and first derivatives of the thermogram curves of the 100 Fe:5 K material at various calcination temperatures are displayed in Figure 3. For all the calcination temperatures investigated in Figure 3, there is a gradual loss of weight from the surface-adsorbed, interstitial, and bulk water of α -Fe₂O₃, with an appreciably strong thermal stability of up to 800 °C.

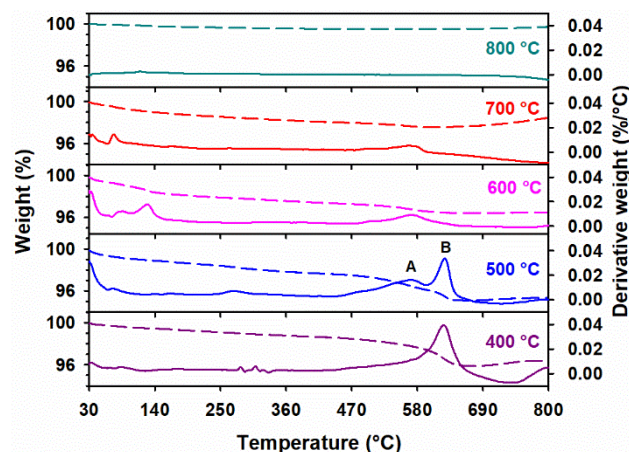


Figure 3. Thermogravimetric analysis (TGA, dashed line with the left vertical axis) and the first derivative of the thermogram (solid line with the right vertical axis) curves for 100 Fe:5 K material, at the calcination temperatures indicated in each panel. Peaks a and B correspond to the conversion of KNO₂ to K₂O, and of KNO₃ to KNO₂, respectively.

Two weight loss regions are identified in Figure 3 for the range of 450–600 °C (peak A) and 600–750 °C (peak B) in the first derivative of the thermogram curve of 100 Fe:5 K material. These two peaks are labeled for the panel at 500 °C in Figure 3, and they correspond to the decomposition of KNO₃ to KNO₂ (peak B at 624.5 °C) and KNO₂ to K₂O (peak a at 568.9 °C) [43–45]. Theoretically, while decomposing, KNO₂ can also recombine with gaseous products (NO₂ and NO) to reform KNO₃ [45,46].

While pure KNO₃ is known to be stable as a liquid (m.p. 334 °C) at least to 530 °C, the presence of a basic metal oxide, such as ZrO₂, was shown to drastically reduce its decomposition temperature, e.g., to 340 °C [47], which is much lower than the temperature range of between 550 and 750 °C that has been used previously to characterize the equilibrium $\text{KNO}_3(l) \rightleftharpoons \text{KNO}_2(l) + \frac{1}{2} \text{O}_2(g)$ [48]. Thus, as the observed decomposition of potassium nitrate on the surface of iron oxide proceeds, peak B drops in size, generating potassium nitrite, which was previously absent in the system. Simultaneously with the previous event, peak a for the now formed potassium nitrite, decomposing into K₂O and NO_x (NO + NO₂), grows [45], to then disappear with all nitrogen species for the materials calcined between 600 and 800 °C.

The assignment of peaks a and B in Figure 3 is supported by similar observations over corundum, with a potassium-doped alumina phase [33]. Although peak B disappears for calcination at 600 °C and 700 °C, the presence of peak a at these temperatures (Figure 3) indicates that KNO₂ is still present. The complete decomposition of KNO₃ and KNO₂ at 800 °C is noticeable in Figure 3. The corresponding thermal stability of the 100 Fe:*x* K materials in the range of $0 \leq x \leq 5$ is reported in the Supplementary Materials (Figure S2), where all K-doped materials that are calcined at 400 °C show similar behavior, as described above.

3.3. Elemental Composition

The results from the ICP-OES analyses, reporting the elemental composition of the materials, are presented in Table 2 and show a good agreement between the experimental composition and the nominal values.

Table 2. Bulk compositional analysis of the materials.

Nominal ^{iv}	Experimental ^v
100 Fe:0 K	100 Fe:0 K
100 Fe:½ K	100 Fe:0.548(2) K
100 Fe:1 K	100 Fe:1.275(3) K
100 Fe:2 K	100 Fe:2.750(5) K
100 Fe:3 K	100 Fe:3.209(13) K
100 Fe:5 K	100 Fe:6.413(56) K

^{iv} Atomic ratio for fixed iron content, ^v from ICP-OES measurements.

3.4. Raman Spectroscopy Analysis

The Raman spectra of the undoped material in Figure 4 show the characteristic peaks (labeled 1 through 8) of the hematite phase in the 100 Fe:*x* K materials for increasing potassium content, calcined at 400 °C. Among these eight peaks for the undoped material, there are two A_{1g} modes centered at 219.3 cm^{-1} (peak 1) and 487.2 cm^{-1} (peak 5), four E_g modes at 244.6 cm^{-1} (peak 2), 281.3 cm^{-1} (peak 3), 400.0 cm^{-1} (peak 4), and 608.2 cm^{-1} (peak 6), one mode for the forbidden E_u mode, showing the presence of disorder in the hematite lattice at 661.8 cm^{-1} (peak 7), and one mode for the two-magnon scattering band centered at 1302.5 cm^{-1} (peak 8) [49–52]. For the K-doped materials, the peaks listed above are slightly shifted. For example, the hematite peaks for 100 Fe:5 K material in Figure 4 are centered at 221.7, 244.3, 286.2, 398.5, 488.0, 597.7, 661.5, and 1312.1 cm^{-1} .

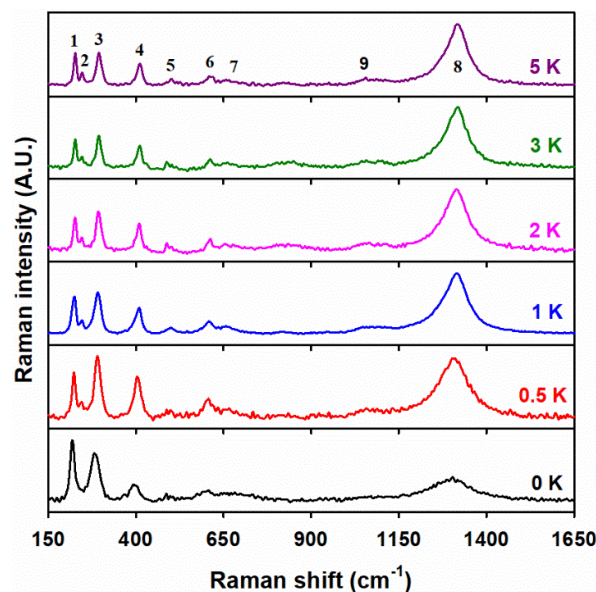


Figure 4. Raman spectra of 100 Fe:*x* K materials, with the atomic ratio of potassium (*x*) indicated in each panel. The numbers 1 to 8 correspond to modes of the hematite phase, while peak 9 relates to a mode of NO_3^- in the range of 980–1150 cm^{-1} .

These shifts could be due to the phonon confinement effects from the nanoscale size of undoped hematite particles with a size of 3.0 nm (observed by TEM, as explained below). a changing chemical bonding effect by the potassium doping is excluded, as no shifts are registered for increasing potassium loadings. The previous observation agrees with the XRD data in Table 1 for the lack of potassium incorporation into the crystal lattice of $\alpha\text{-Fe}_2\text{O}_3$. Figure 4 also confirms the presence of KNO_3 in the doped materials, as evidenced by the Raman mode at 1055 cm^{-1} (peak 9) from the symmetric stretching vibration of NO_3^- [53]. Peak 9 becomes notable only in the 100 Fe:½ K material and increases its intensity for

higher potassium loading. The Raman spectra for 100 Fe:5 K material calcined at higher temperatures, which are displayed in Figure S3 (Supplementary Materials), show that peak 9 starts to drop its intensity at 600 °C, and completely disappears at 700 °C. No change in the band position of the hematite peaks occurs for the increasing calcination temperature. No vibrational features for K₂O or K₂Fe₂₂O₃₄ could be observed by Raman spectroscopy due to the limitations of the technique, which are overcome by surface-sensitive XPS analysis.

3.5. XPS Analysis

The surface composition of undoped and K-doped α -Fe₂O₃ after calcination at various temperatures is provided by XPS analysis. Qualitative elemental analysis is possible due to our analyzing the surveyed and high-resolution XPS spectra, which yield the electronic state and chemical bonding of the elements. For example, the XPS survey spectra for 100 Fe:*x* K for *x* = 0, 1, and 5 are shown in Figure 5. While undoped α -Fe₂O₃ only shows oxygen and iron (disregarding the presence of signals from adventitious carbon), the doped materials (e.g., for 1 K and 5 K in Figure 5) additionally display the presence of potassium; however, the nitrogen signals are too small and are only detected in the high-resolution XPS spectra. The left panel of Figure 6 shows the high-resolution XPS spectra for O 1s, with peaks centered at 529.3, 530.9, and 531.5 eV in the 100 Fe:0 K material, corresponding to the lattice oxygen binding with Fe(III) (denoted as Fe–O and labeled as peak 1) in α -Fe₂O₃, lattice hydroxyl (peak 2), and surface hydroxyl (peak 3), respectively.

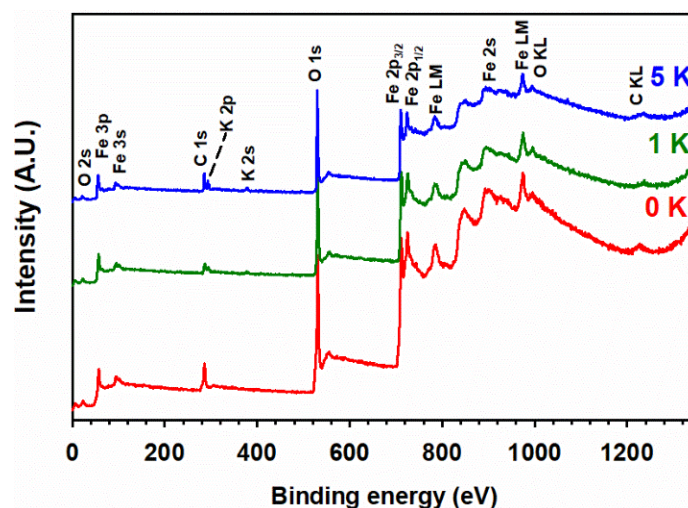


Figure 5. X-ray photoelectron (XPS) survey spectra for 100 Fe:*x* K materials with *x* = 0, 1, and 5, as indicated by the red, green, and blue traces, respectively. The peak assignment is based on the binding energy of photoelectron and Auger electron lines.

With K-doping, the O 1s XPS spectra do not show any new features of oxygen related to a possible K–O bond. The high-resolution XPS spectra of Fe 2*p* (right panel in Figure 6) show two distinct, intense peaks at the binding energies of 710.1 eV and 723.5 eV, which correspond to Fe 2*p*_{3/2} (peak 4) and Fe 2*p*_{1/2} (peak 6), respectively. The doublet (peaks 4 and 6) arises due to the spin-orbit coupling in the Fe 2*p* states. There are also two additional satellite peaks at binding energies of 718.0 eV and 732.1 eV, assigned to Fe 2*p*_{3/2} (peak 5) and Fe 2*p*_{1/2} (peak 7), respectively. These features of Fe 2*p* are in good agreement with the Fe(III) states reported for α -Fe₂O₃ (hematite) [41,54,55]. The presence of Fe(II) 2*p* states was discarded, as there are neither spin-orbit splitting nor satellite peaks for Fe(II) states in both doped and undoped materials. The binding energies of peaks 1–7 are not shifted in the K-doped materials, discarding the incorporation of potassium into the lattice of α -Fe₂O₃.

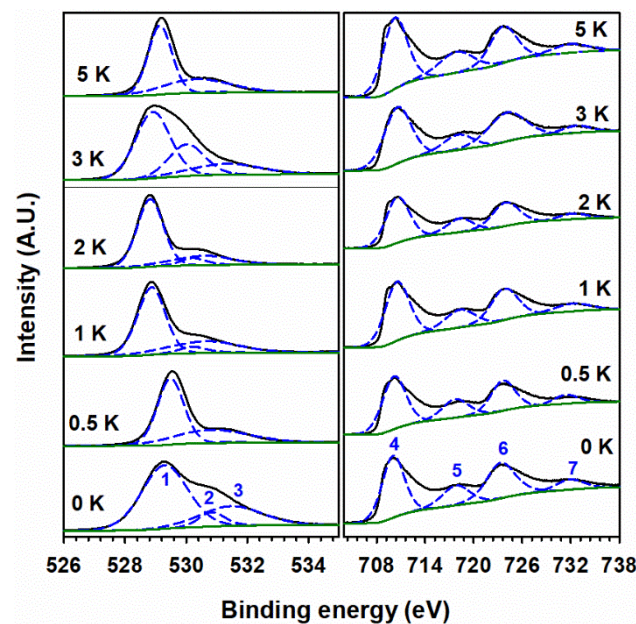


Figure 6. (Black trace) High-resolution XPS spectra of (left panel) O 1s and (right panel) Fe(III) 2p for 100 Fe:*x* K materials, calcined at 400 °C, with the atomic ratio of potassium (*x*) indicated in each panel. Dashed blue lines show the fitted peaks, numbered as follows: (1) O 1s for lattice oxides, (2) lattice hydroxyl, (3) surface hydroxyl, (4) Fe(III) 2p_{3/2}, (5) Fe 2p_{3/2} satellite, (6) Fe(III) 2p_{1/2}, and (7) Fe(III) 2p_{1/2} satellite. Solid green lines show the fitted background.

The high-resolution XPS spectra for potassium in the left panel of Figure 7 show two peaks at the binding energies of 292.7 and 295.4 eV for K 2p_{3/2} (peak 8) and K 2p_{1/2} (peak 9), respectively. The binding energy difference of 2.7 eV for peaks 8 and 9 is due to the spin-orbit coupling of potassium cations in potassium nitrates [56]. No systematic shift in the binding energy of K 2p has been observed in these spectra, which indicates that the added potassium is not interacting chemically with α-Fe₂O₃. The presence of nitrate, remaining at this low calcination temperature, is also confirmed in the high-resolution XPS spectra for nitrogen (right panel of Figure 7) by peak 10 at 406.8 eV [57]. Peak 10 is hard to perceive in the 100 Fe: $\frac{1}{2}$ K material because of the very low concentration of nitrogen that is nominally present as KNO₃.

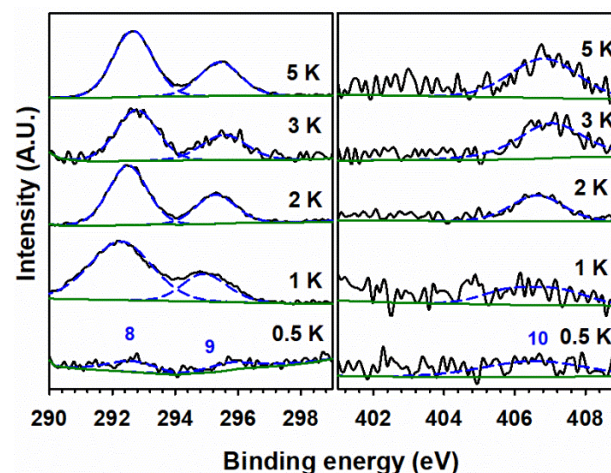


Figure 7. (Black trace) High-resolution XPS spectra of (left panel) K 2p and (right panel) N 1s for 100 Fe:*x* K materials, calcined at 400 °C, with the atomic ratio of potassium (*x*) indicated in each panel. (Dashed blue) Fitted peaks numbered (8) K 2p_{3/2}, (9) K 2p_{1/2}, and (10) nitrate. (Solid green) Fitted background.

The observation of peak 10 for nitrate in these doped materials indicates that KNO_3 did not decompose when calcined at 400°C . Figure 8 presents high-resolution XPS spectra for 100 Fe:5 K with K $2p$ (peaks 8 and 9) and N $1s$ (peak 10, for nitrate) signals at various calcination temperatures. Peak 10 is observed at 400, 500, and 600°C . In addition, a peak at 402.8 eV for the nitrite (peak 11) [57] is clearly observed at 500°C , confirming its production as a result of the decomposition of nitrate. The binding energies of peaks for spin-orbit coupling and their corresponding satellite peaks of Fe $2p$ neither show a shift with calcination temperature nor demonstrate the presence of new peaks in the high-resolution XPS spectra (Figure S4, Supplementary Materials). Thus, the starting hematite phase is maintained by $\alpha\text{-Fe}_2\text{O}_3$ for all calcination temperatures and compositions, but a solid solution is formed at 800°C , as evidenced by the peaks marked with a red cross in Figure 2. Even at 800°C (Figure S4, Supplementary Materials), no change in the oxidation state of iron is registered by XPS. However, a small contribution of iron(II) $2p$ [58] may be observed in the high-resolution XPS spectra for the samples calcined at 500°C and 600°C (Figure S4, Supplementary Materials). Calcination at higher temperatures can create oxygen vacancies in the iron oxide lattice, which leaves two electrons per oxygen atom [59]. Therefore, the introduction of two electrons can reduce iron(III) to iron(II). The absence of any nitrogen-bonded species in the right panel of Figure 8 proves that the complete decomposition of KNO_3 and KNO_2 occurs at 700°C and 800°C , which produces K_2O and $\text{K}_2\text{Fe}_{22}\text{O}_{34}$ (as seen in Figure 2). The hypothetical production of metallic potassium at high calcination temperature is discarded as no K $2p$ doublet, for K $2p_{3/2}$ and K $2p_{1/2}$, is registered at 295 and 298 eV, respectively [56]. The O $1s$ fitting for the sample calcined at various temperatures is shown in Figure 9. The peak fitting was carried out by keeping the full-width half-maximum of the lattice iron oxygen constant in all calcined materials [60]. an additional peak at lower binding energy could be assigned to the potassium-bonded oxygen species (K–O), likely provided by NO_3^- , in the doped samples. Table S1 (Supplementary Materials) provides the surface ratio of potassium to iron content in experiments under variable potassium loading and calcination temperatures, which value is obtained by the integration of the areas under the fitted peaks for K $2p_{3/2}$ and Fe $2p_{3/2}$ in XPS in Figures 6–8.

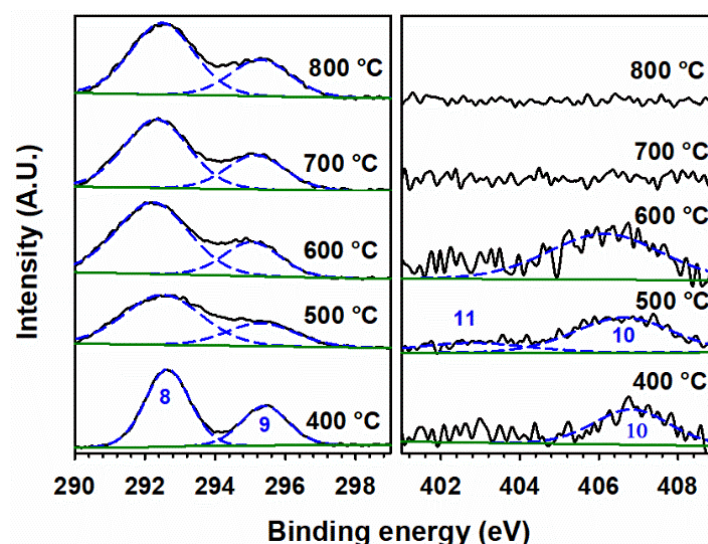


Figure 8. (Black trace) High-resolution XPS spectra of (left panel) K $2p$ and (right panel) N $1s$ for 100 Fe:5 K material, calcined at the indicated temperatures. (Dashed blue) Fitted peaks numbered (8) K $2p_{3/2}$, (9) K $2p_{1/2}$, (10) nitrate, and (11) nitrite. (Solid green) Fitted background.

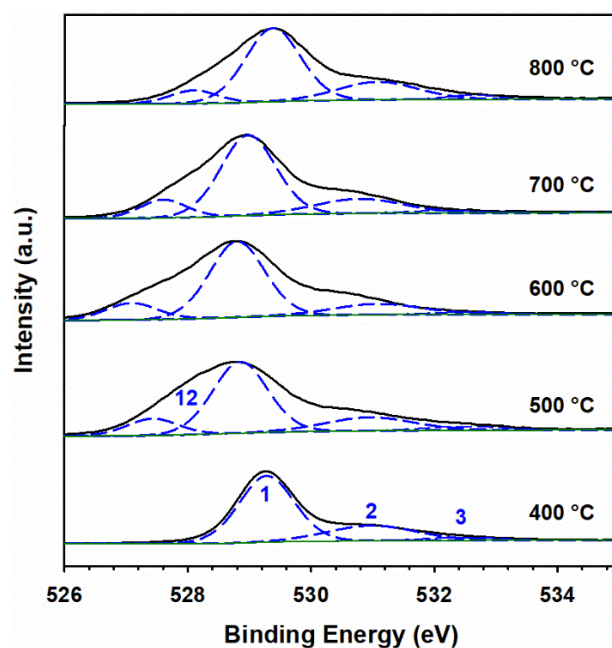


Figure 9. (Black trace) High-resolution XPS spectra of O 1s for 100 Fe:5 K material, calcined at the temperature specified in each panel. (Dashed blue) Fitted peaks numbered (1) O 1s for lattice iron oxides, (2) lattice hydroxyl, (3) surface hydroxyl, and (12) K–O bonded species. (Solid green) Fitted background.

3.6. TEM and EDS Analyses

The size, morphology, and microstructure of the materials are characterized using TEM and high-resolution TEM (HR-TEM). Individual hexagonal particles of undoped and K-doped α -Fe₂O₃ are shown in Figure 10. The particle sizes of the materials in Figure 10 are reported in Table 3, based on the distribution analysis of individual particles in the histograms in Figure S5 (Supplementary Materials). For undoped α -Fe₂O₃, the average diameter of the particles is about 2.56 nm.

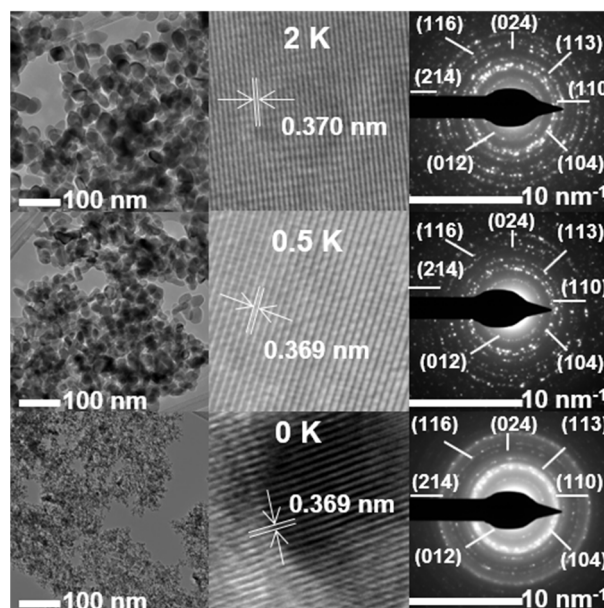


Figure 10. (From left to right) Transmission electron microscopy (TEM), high-resolution TEM (HRTEM), and selected area electron diffraction (SAED) patterns of (from top to bottom) 100 Fe:2 K, 100 Fe:½ K, and 100 Fe:0 K materials, calcined at 400 °C.

Table 3. The average diameter of α -Fe₂O₃ particles and surface potassium content (x) for selected materials and calcination temperatures (T).

Material	T (°C)	Diameter (nm) ^{vi}	χ ^{vii}
100 Fe:0 K	400	2.56	0.00
100 Fe: $\frac{1}{2}$ K	400	15.4	0.48
100 Fe:2 K	400	17.5	0.85
100 Fe:5 K	400	17.6	0.93
100 Fe:5 K	600	20.0	2.80
100 Fe:5 K	800	135.3	1.43

^{vi} Diameter calculated from the Gaussian fittings in the histogram obtained from TEM images. ^{vii} Potassium content from the integration of K(K α) line in the EDS spectra.

The undoped particles in Figure 10, with an average particle diameter of 2.51 nm, grow to 15.2 and 17.4 nm after the addition of $\frac{1}{2}$ K and 2 K, respectively (Table 3), without any further significant change for 5 K when the calcination was 400 °C. The increase in particle size indicates that the addition of potassium results in larger crystals. This observed behavior by TEM (Table 3) follows the same trend for the crystallite size obtained by XRD (Table 1). The HRTEM images show good crystallization, with well-defined lattice fringes at an interplanar spacing of 0.369 nm, which is consistent with a d_{012} of α -Fe₂O₃ within ± 0.002 nm for the materials with or without potassium (Figure S6, Supplementary Materials). These d_{012} values correspond to the reciprocal of the radius of each diffraction ring in the SAED patterns and are in excellent agreement with the X-ray crystallographic data (JCPDS #033-0664 with $d_{012} = 0.368$ nm). In addition, the interplanar spacings of other major diffraction peaks remain unchanged for both undoped and doped materials (Figure S6, Supplementary Materials). Furthermore, the SAED patterns (Figure 10) only show the continuous ring patterns for the α -Fe₂O₃ phase, without any additional diffraction spots and rings, even after potassium doping.

Table 3 also reports the potassium contents on the surface of the materials, which are obtained during TEM by EDS analysis, followed by the integration of the peak areas. For low-potassium doping, the experimental composition of the surface is close to the nominal value (Table 3), but for increasing nominal potassium content, there is a significant deviation due to heterogeneous doping.

The compositional analysis of iron and potassium using ICP-OES matches the nominal content. However, the EDS analysis shows a significant deviation from the nominal values. As described earlier in XRD and Raman analysis, potassium ion is not incorporated into the iron oxide lattice due to the larger size of K⁺ than Fe³⁺. Therefore, potassium ions reside on the surface of iron oxide. Thus, such a deviation of potassium content in EDS analysis relative to the nominal composition may simply reflect a limitation of this technique. Moreover, during EDS analysis, potassium content was calculated from selected heterogeneous particles that, on average, have a lower potassium content than iron content. Hence, EDS provides more qualitative information about the potassium content [61,62] than ICP-OES. On the other hand, ICP-OES analyzes the bulk potassium content. Therefore, the results from ICP-OES represent the most reliable quantitative information [63]. Figure 11 shows examples for the increasing potassium content on the surface of 100 Fe: x K for $x = 0, \frac{1}{2},$ and 5 K, as registered by EDS for the K (K α) line. TEM images for 100 Fe:5 K material calcined at various temperatures are displayed in Figure 12, and the corresponding analysis of their size distribution is provided in Table 3 and Figure S5 (Supplementary Materials). The larger particle size, with increasing calcination temperature, is simply due to the agglomeration of particles. At the microscopic level, the high temperature enlarges the grain boundaries and improves mass transport, consequently allowing the particles to grow.

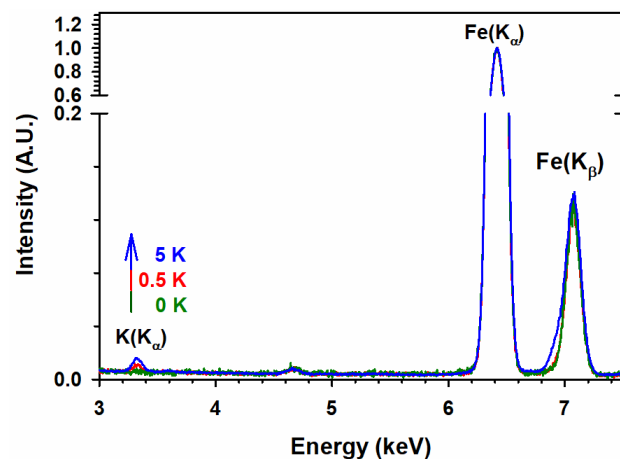


Figure 11. Energy-dispersive X-ray spectroscopy (EDS) spectra of 100 Fe:*x* K materials for potassium contents (*x*) of (green) 0 K, (red) $\frac{1}{2}$ K, and (blue) 5 K for the K ($K\alpha$) emission line.

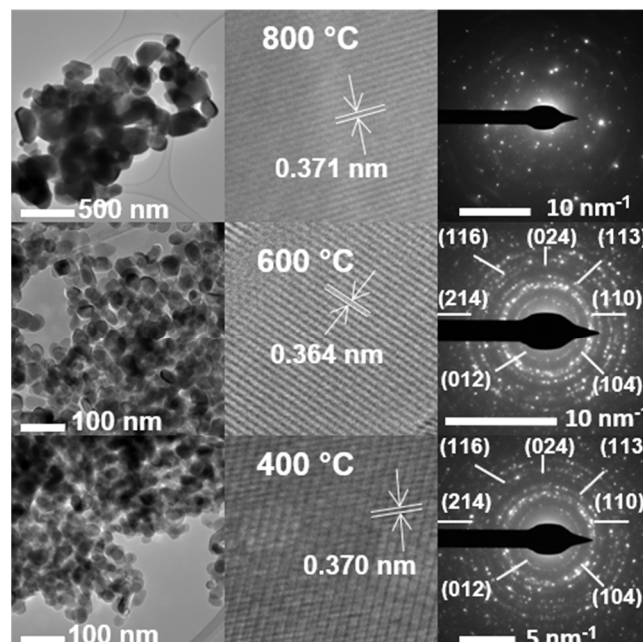


Figure 12. (From left to right) TEM, HRTEM, and SAED patterns of 100 Fe:5 K calcined at (from top to bottom), 800, 600, and 400 °C.

At the macroscopic level, the increase in particle size can be ascribed to the reduction in total surface energy caused by the calcination temperature. The calcined 100 Fe:5 K material retains the hematite phase up to 700 °C (see the XRD and Raman spectra above) without forming any new phase, as shown in the SAED patterns, for example at 600 °C in Figure 12, with unchanged interplanar spacings. The SAED patterns also reflect the polycrystallinity of the materials. For calcination at 800 °C, it was impossible to observe any clear rings in the SAED spectrum of 100 Fe:5 K, due to the large, agglomerated crystals. However, the few SAED spots that could still be assigned at 800 °C are accurately indexed by the hematite phase of α -Fe₂O₃.

4. Conclusions

The hematite phase of the materials remains stable upon the addition of potassium nitrate for iron oxide, with atomic compositions as high as 100 Fe:5 K up to 700 °C. However, XRD confirms that at 800 °C, two new phases are formed, K₂O and K₂Fe₂₂O₃₄. The transformation of KNO₃ into KNO₂ starts at 500 °C, and these species completely decompose

at 800 °C. The current study verifies the finding that the remaining potassium produces K₂O at 700 and 800 °C. This work confirms the importance of studying the chemical and electronic states of alkali metals such as potassium dopants in the host materials before using them as catalysts. We recommend the 100 Fe:5 K material calcined at 800 °C for catalytic applications of K₂O/ α -Fe₂O₃. Future work with potassium nitrate-doped iron oxide in the catalysis and photocatalysis fields can potentially improve multiple processes, if explored carefully, by ensuring the state of potassium species.

Supplementary Materials: The following supporting information can be downloaded at: <https://www.mdpi.com/article/10.3390/ma15207378/s1>, Additional experimental methods, additional results, and discussion; and Figures S1–S10 and Table S1 are in the Supplementary Materials files. References [64,65] are cited in the Supplementary Materials files.

Author Contributions: Conceptualization, M.A.H. and M.I.G.; methodology, M.A.H., M.I.G., J.P.S. and M.K.G.; formal analysis, M.A.H. and M.I.G.; investigation, M.A.H. and M.I.G.; resources, M.I.G., J.P.S. and M.K.G.; data curation, M.A.H. and M.I.G.; writing—original draft preparation, M.A.H. and M.I.G.; writing—review and editing, M.A.H., M.I.G., J.P.S. and M.K.G.; visualization, M.A.H. and M.I.G.; supervision, M.I.G.; project administration, M.I.G.; funding acquisition, M.I.G. All authors have read and agreed to the published version of the manuscript.

Funding: This research was supported by the USA NSF grant number 1903744. The APC was funded by MDPI Materials.

Institutional Review Board Statement: Not applicable.

Informed Consent Statement: Not applicable.

Data Availability Statement: The data presented in this study are available upon reasonable request from the corresponding author.

Acknowledgments: We thank research funding from the USA National Science Foundation award 1903744 to M.I.G. Partial support from the University of Kentucky by A Research Challenge Trust Fund Fellowship to M.A.H. is gratefully acknowledged.

Conflicts of Interest: The authors declare no conflict of interest. The funders had no role in the design of the study; in the collection, analyses, or interpretation of data; in the writing of the manuscript; or in the decision to publish the results.

Abbreviations

DSC, Differential Scanning Calorimetry; ICP-OES, Inductively Coupled Plasma-Optical Emission Spectroscopy; IWIM, Incipient Wetness Impregnation Method; SAED, Selected Area Electron Diffraction; TEM, Transmission Electron Microscopy; TGA Thermogravimetric Analysis; XRD, X-ray Diffraction; XPS, X-ray Photoelectron Spectroscopy.

References

1. Fischer, F.; Tropsch, H. The Synthesis of Petroleum at Atmospheric Pressures from Gasification Products of Coal. *Brennst. Chem.* **1926**, *7*, 97–104.
2. Fischer, F.; Tropsch, H. The Preparation of Synthetic oil Mixtures (Synthol) from Carbon Monoxide and Hydrogen. *Brennst. Chem.* **1923**, *4*, 276–285.
3. Govender, N.; de Croon, M.; Schouten, J.C. Reactivity of Surface Carbonaceous Intermediates on an Iron-based Fischer–Tropsch Catalyst. *Appl. Catal. A Gen.* **2010**, *373*, 81–89. [[CrossRef](#)]
4. Benziger, J.; Madix, R. The effects of Carbon, Oxygen, Sulfur and Potassium Adlayers on CO and H₂ Adsorption on Fe(100). *Surf. Sci.* **1980**, *94*, 119–153. [[CrossRef](#)]
5. Dry, M.; Shingles, T.; Boshoff, L.; Oosthuizen, G.J. Heats of Chemisorption on Promoted Iron Surfaces and the Role of Alkali in Fischer-Tropsch Synthesis. *J. Catal.* **1969**, *15*, 190–199. [[CrossRef](#)]
6. Amelse, J.; Butt, J.; Schwartz, L. Carburization of Supported Iron Synthesis Catalysts. *J. Phys. Chem.* **1978**, *82*, 558–563. [[CrossRef](#)]
7. Bukur, D.B.; Mukesh, D.; Patel, S.A. Promoter Effects on Precipitated Iron Catalysts for Fischer-Tropsch Synthesis. *Ind. Eng. Chem. Res.* **1990**, *29*, 194–204. [[CrossRef](#)]

8. Arakawa, H.; Bell, A.T. Effects of Potassium Promotion on the Activity and Selectivity of Iron Fischer-Tropsch Catalysts. *Ind. Eng. Chem. Process Des. Dev.* **1983**, *22*, 97–103. [[CrossRef](#)]
9. Yang, Y.; Xiang, H.; Xu, Y.; Bai, L.; Li, Y. Effect of Potassium Promoter on Precipitated Iron-Manganese Catalyst for Fischer-Tropsch Synthesis. *Appl. Catal. A Gen.* **2004**, *266*, 181–194. [[CrossRef](#)]
10. Storch, H.H. The Fischer-Tropsch and Related Processes for Synthesis of Hydrocarbons by Hydrogenation of Carbon Monoxide. In *Advances in Catalysis*; Frankenburg, W.G., Komarewsky, V.I., Rideal, E.K., Eds.; Academic Press: New York, NY, USA, 1948; Volume 1, pp. 115–156.
11. Cho, J.; Jeong, M.; Bae, J. Fischer-Tropsch Synthesis on Potassium-Modified FeO Nanoparticles. *Res. Chem. Intermed.* **2016**, *42*, 335–350. [[CrossRef](#)]
12. Liu, B.; Li, W.; Zheng, J.; Lin, Q.; Zhang, X.; Zhang, J.; Jiang, F.; Xu, Y.; Liu, X. CO₂ Formation Mechanism in Fischer-Tropsch Synthesis Over Iron-based Catalysts: A Combined Experimental and Theoretical Study. *Catal. Sci. Technol.* **2018**, *8*, 5288–5301. [[CrossRef](#)]
13. Pendyala, V.R.R.; Graham, U.M.; Jacobs, G.; Hamdeh, H.H.; Davis, B.H. Fischer-Tropsch Synthesis: Deactivation as a Function of Potassium Promoter Loading for Precipitated Iron Catalyst. *Catal. Lett.* **2014**, *144*, 1704–1716. [[CrossRef](#)]
14. Asano, K.; Ohnishi, C.; Iwamoto, S.; Shioya, Y.; Inoue, M. Potassium-doped Co₃O₄ Catalyst for Direct Decomposition of N₂O. *Appl. Catal. B Environ.* **2008**, *78*, 242–249. [[CrossRef](#)]
15. Tang, X.; Gao, F.; Xiang, Y.; Yi, H.; Zhao, S.; Liu, X.; Li, Y. Effect of Potassium-Precursor Promoters on Catalytic Oxidation Activity of Mn-CoO_x Catalysts for NO Removal. *Ind. Eng. Chem. Res.* **2015**, *54*, 9116–9123. [[CrossRef](#)]
16. Solís-Casados, D.; Escobar, J.; Orozco, I.G.; Klimova, T. Effect of Potassium Content on the Performance of CoMo/Al₂O₃-MgO-K₂O(x) Catalysts in Hydrodesulfurization of Dibenzothiophene. *Ind. Eng. Chem. Res.* **2011**, *50*, 2755–2761. [[CrossRef](#)]
17. Tian, S.; Wang, S.; Wu, Y.; Gao, J.; Wang, P.; Xie, H.; Yang, G.; Han, Y.; Tan, Y. The Role of Potassium Promoter in Isobutanol Synthesis over Zn-Cr Based Catalysts. *Catal. Sci. Technol.* **2016**, *6*, 4105–4115. [[CrossRef](#)]
18. Cheng, Y.; Lin, J.; Wu, T.; Xie, S.; Pei, Y.; Yan, S.; Qiao, M.; Zong, B. Mg and K Dual-Decorated Fe-on-Reduced Graphene Oxide for Selective Catalyzing CO Hydrogenation to Light Olefins with Mitigated CO₂ Emission and Enhanced Activity. *Appl. Catal. B Environ.* **2017**, *204*, 475–485. [[CrossRef](#)]
19. Saththawong, R.; Koizumi, N.; Song, C.; Prasassarakich, P. Light Olefin Synthesis from CO₂ Hydrogenation Over K-Promoted Fe-Co Bimetallic Catalysts. *Catal. Today* **2015**, *251*, 34–40. [[CrossRef](#)]
20. Lohitharn, N.; Goodwin, J.G. Effect of K Promotion of Fe and FeMn Fischer-Tropsch Synthesis Catalysts: Analysis at the Site Level Using SSITKA. *J. Catal.* **2008**, *260*, 7–16. [[CrossRef](#)]
21. Jiang, F.; Zhang, M.; Liu, B.; Xu, Y.; Liu, X. Insights Into the Influence of Support and Potassium or Sulfur Promoter on Iron-Based Fischer-Tropsch Synthesis: Understanding the Control of Catalytic Activity, Selectivity to Lower Olefins, and Catalyst Deactivation. *Catal. Sci. Technol.* **2017**, *7*, 1245–1265. [[CrossRef](#)]
22. Maniak, G.; Stelmachowski, P.; Kotarba, A.; Sojka, Z.; Rico-Pérez, V.; Bueno-López, A. Rationales for the Selection of the Best Precursor for Potassium Doping of Cobalt Spinel Based de N₂O Catalyst. *Appl. Catal. B Environ.* **2013**, *136–137*, 302–307. [[CrossRef](#)]
23. Mavlyankariev, S.; Ahlers, S.; Kondratenko, V.; Linke, D.; Kondratenko, E. Effect of Support and Promoter on Activity and Selectivity of Gold Nanoparticles in Propanol Synthesis from CO₂, C₂H₄ and H₂. *ACS Catal.* **2016**, *6*, 3317–3325. [[CrossRef](#)]
24. Shi, Z.; Yang, H.; Gao, P.; Li, X.; Zhong, L.; Wang, H.; Liu, H.; Wei, W.; Sun, Y. Direct Conversion of CO₂ to Long-Chain Hydrocarbon Fuels over K-Promoted CoCu/TiO₂ Catalysts. *Catal. Today* **2018**, *311*, 65–73. [[CrossRef](#)]
25. Li, J.; Cheng, X.; Zhang, C.; Dong, W.; Yang, Y.; Li, Y. Comparative Study of Iron-Based Fischer-Tropsch Synthesis Catalysts Promoted with Strontium or Potassium. *Catal. Lett.* **2016**, *146*, 2574–2584. [[CrossRef](#)]
26. Priyanka; Srivastava, V.C. Photocatalytic Oxidation of Dye Bearing Wastewater by Iron Doped Zinc Oxide. *Ind. Eng. Chem. Res.* **2013**, *52*, 17790–17799. [[CrossRef](#)]
27. Ma, Z.; Liu, G.; Lu, Y.; Zhang, H. Redox performance of Fe₂O₃/Al₂O₃ oxygen carrier calcined at different temperature in chemical looping process. *Fuel* **2022**, *310*, 122381. [[CrossRef](#)]
28. Xu, X.; Zhang, Q.; Wu, J.; Zhang, Z.; Wei, P.; Liu, Y. Effect of Fe₂O₃-TiO₂-Sm₂O₃ composite additive on sintering behavior and thermal properties of Al₂O₃ ceramics for thermal storage. *Ceram. Int.* **2022**, *48*, 11356–11364. [[CrossRef](#)]
29. Niu, M.-S.; Yang, H.-H.; Zhou, H.; Yi, X.; Zhou, X.; Zhan, J.; Liu, Y. Synergy of the successive modification of cryptomelane MnO₂ by potassium insertion and nitrogen doping for catalytic formaldehyde oxidation. *Chem. Eng. J.* **2022**, *431*, 133928. [[CrossRef](#)]
30. Kharlamova, T.S.; Verkhov, V.A.; Kulchakovskaya, E.V.; Svetlichnyi, V.A.; Cadete Santos Aires, F.J.; Bargiela, P.; Vodyankina, O.V. Effect of metal-doping (Me = Fe, Ce, Sn) on phase composition, structural peculiarities, and CO oxidation catalytic activity of cryptomelane-type MnO₂. *J. Alloys Compd.* **2022**, *917*, 165504. [[CrossRef](#)]
31. Lyu, Z.; Niu, S.; Han, K.; Lu, C.; Li, Y. Theoretical insights into the poisoning effect of Na and K on α -Fe₂O₃ catalyst for selective catalytic reduction of NO with NH₃. *Appl. Catal. A Gen.* **2021**, *610*, 117968. [[CrossRef](#)]
32. Gu, M.; Dai, S.; Qiu, R.; Ford, M.E.; Cao, C.; Wachs, I.E.; Zhu, M. Structure-Activity Relationships of Copper- and Potassium-Modified Iron Oxide Catalysts during Reverse Water-Gas Shift Reaction. *ACS Catal.* **2021**, *11*, 12609–12619. [[CrossRef](#)]
33. Tian, P.; Gu, M.; Qiu, R.; Yang, Z.; Xuan, F.; Zhu, M. Tunable Carbon Dioxide Activation Pathway over Iron Oxide Catalysts: Effects of Potassium. *Ind. Eng. Chem. Res.* **2021**, *60*, 8705–8713. [[CrossRef](#)]

34. Barrios, A.J.; Peron, D.V.; Chakkingal, A.; Dugulan, A.I.; Moldovan, S.; Nakouri, K.; Thuriot-Roukos, J.; Wojcieszak, R.; Thybaut, J.W.; Virginie, M.; et al. Efficient Promoters and Reaction Paths in the CO₂ Hydrogenation to Light Olefins over Zirconia-Supported Iron Catalysts. *ACS Catal.* **2022**, *12*, 3211–3225. [[CrossRef](#)]
35. Liu, J.; Cheng, H.; Zheng, H.; Zhang, L.; Liu, B.; Song, W.; Liu, J.; Zhu, W.; Li, H.; Zhao, Z. Insight into the Potassium Poisoning Effect for Selective Catalytic Reduction of NO_x with NH₃ over Fe/Beta. *ACS Catal.* **2021**, *11*, 14727–14739. [[CrossRef](#)]
36. Al Maksoud, W.; Rai, R.K.; Morlanés, N.; Harb, M.; Ahmad, R.; Ould-Chikh, S.; Anjum, D.; Hedhili, M.N.; Al-Sabban, B.E.; Albahily, K.; et al. Active and stable Fe-based catalyst, mechanism, and key role of alkali promoters in ammonia synthesis. *J. Catal.* **2021**, *394*, 353–365. [[CrossRef](#)]
37. Chang, H.; Lin, Q.; Cheng, M.; Zhang, K.; Feng, B.; Chai, J.; Lv, Y.; Men, Z. Effects of Potassium Loading over Iron–Silica Interaction, Phase Evolution and Catalytic Behavior of Precipitated Iron-Based Catalysts for Fischer-Tropsch Synthesis. *Catalysts* **2022**, *12*, 916. [[CrossRef](#)]
38. Folke, J.; Dembélé, K.; Girgsdies, F.; Song, H.; Eckert, R.; Reitmeier, S.; Reitzmann, A.; Schlögl, R.; Lunkenbein, T.; Ruland, H. Promoter effect on the reduction behavior of wuestite-based catalysts for ammonia synthesis. *Catal. Today* **2022**, *387*, 12–22. [[CrossRef](#)]
39. Xu, M.; Cao, C.; Xu, J. Understanding kinetically interplaying reverse water-gas shift and Fischer-Tropsch synthesis during CO₂ hydrogenation over Fe-based catalysts. *Appl. Catal. A Gen.* **2022**, *641*, 118682. [[CrossRef](#)]
40. DeLaHunt, J.S.; Lindeman, T.G. Review of the safety of potassium and potassium oxides, including deactivation by introduction into water. *J. Chem. Health Saf.* **2007**, *14*, 21–32. [[CrossRef](#)]
41. Wang, R.; Xu, C.; Sun, J.; Gao, L. Three-Dimensional Fe₂O₃ Nanocubes/Nitrogen-doped Graphene Aerogels: Nucleation Mechanism and Lithium Storage Properties. *Sci. Rep.* **2014**, *4*, 7171. [[CrossRef](#)]
42. Markus, Y. (Ed.) *Ion Properties*; Marcel Dekker: New York, NY, USA, 1997.
43. Kramer, C.M.; Munir, Z.A.; Volponi, J.V. Differential Scanning Calorimetry of Sodium and Potassium Nitrates and Nitrites. *Thermochim. Acta* **1982**, *55*, 11–17. [[CrossRef](#)]
44. Freeman, E.S. The Kinetics of the Thermal Decomposition of Potassium Nitrate and of the Reaction between Potassium Nitrite and Oxygen. *J. Am. Chem. Soc.* **1957**, *79*, 838–842. [[CrossRef](#)]
45. Stern, K.H. High Temperature Properties and Decomposition of Inorganic Salts part 3, Nitrates and Nitrites. *J. Phys. Chem. Ref. Data* **1972**, *1*, 747–772. [[CrossRef](#)]
46. Oza, T.M. Thermal Decomposition of Sodium and Potassium Nitrites. *J. Indian Chem. Soc.* **1945**, *22*, 173–180.
47. Wang, Y.; Huang, W.Y.; Chun, Y.; Xia, J.R.; Zhu, J.H. Dispersion of Potassium Nitrate and the Resulting Strong Basicity on Zirconia. *Chem. Mater.* **2001**, *13*, 670–677. [[CrossRef](#)]
48. Bartholomew, R.F. A Study of the Equilibrium $\text{KNO}_3(l) \rightleftharpoons \text{KNO}_2(l) + 1/2\text{O}_2(g)$ over the Temperature Range 550–750°. *J. Phys. Chem.* **1966**, *70*, 3442–3446. [[CrossRef](#)]
49. Chernyshova, I.V.; Hochella Jr, M.F.; Madden, A.S. Size-dependent Structural Transformations of Hematite Nanoparticles. 1. Phase Transition. *Phys. Chem. Chem. Phys.* **2007**, *9*, 1736–1750. [[CrossRef](#)]
50. Jubb, A.M.; Allen, H.C. Vibrational Spectroscopic Characterization of Hematite, Maghemite, and Magnetite Thin Films Produced by Vapor Deposition. *ACS Appl. Mater. Interfaces* **2010**, *2*, 2804–2812. [[CrossRef](#)]
51. Bersani, D.; Lottici, P.P.; Montenero, A. Micro-Raman Investigation of Iron Oxide Films and Powders Produced by Sol–Gel Syntheses. *J. Raman Spectrosc.* **1999**, *30*, 355–360. [[CrossRef](#)]
52. Chourpa, I.; Douziech-Eyrolles, L.; Ngaboni-Okassa, L.; Fouquenot, J.; Cohen-Jonathan, S.; Soucé, M.; Marchais, H.; Dubois, P. Molecular Composition of Iron Oxide Nanoparticles, Precursors for Magnetic Drug Targeting, as Characterized by Confocal Raman Microspectroscopy. *Analyst* **2005**, *130*, 1395–1403. [[CrossRef](#)]
53. Brooker, M.H.; Irish, D.E. Infrared and Raman Spectral Studies of KNO₂–KNO₃ Solutions. *Can. J. Chem.* **1968**, *46*, 229–233. [[CrossRef](#)]
54. Kraushofer, F.; Jakub, Z.; Bichler, M.; Hulva, J.; Drmota, P.; Weinold, M.; Schmid, M.; Setvin, M.; Diebold, U.; Blaha, P.; et al. Atomic-Scale Structure of the Hematite $\alpha\text{-Fe}_2\text{O}_3(1\bar{1}02)$ “R-Cut” Surface. *J. Phys. Chem. C* **2018**, *122*, 1657–1669. [[CrossRef](#)] [[PubMed](#)]
55. Yamashita, T.; Hayes, P. Effect of Curve Fitting Parameters on Quantitative Analysis of Fe_{0.94}O And Fe₂O₃ using XPS. *J. Electron Spectrosc. Relat. Phenom.* **2006**, *152*, 6–11. [[CrossRef](#)]
56. Jolm, F.M.; William, F.S.; Peter, E.S.; Kennetlf, D.B. *Handbook of X-ray Photoelectron Spectroscopy*; Perkin-Elmer Corporation: Eden Prairie, MN, USA, 1992.
57. Nanayakkara, C.E.; Jayaweera, P.M.; Rubasinghege, G.; Baltrusaitis, J.; Grassian, V.H. Surface Photochemistry of Adsorbed Nitrate: The Role of Adsorbed Water in the Formation of Reduced Nitrogen Species on $\alpha\text{-Fe}_2\text{O}_3$ Particle Surfaces. *J. Phys. Chem. A* **2014**, *118*, 158–166. [[CrossRef](#)]
58. Biesinger, M.C.; Payne, B.P.; Grosvenor, A.P.; Lau, L.W.M.; Gerson, A.R.; Smart, R.S.C. Resolving Surface Chemical States in XPS Analysis of First Row Transition Metals, Oxides and Hydroxides: Cr, Mn, Fe, Co and Ni. *Appl. Surf. Sci.* **2011**, *257*, 2717–2730. [[CrossRef](#)]
59. Rioult, M.; Stanescu, D.; Fonda, E.; Barbier, A.; Magnan, H. Oxygen Vacancies Engineering of Iron Oxides Films for Solar Water Splitting. *J. Phys. Chem. C* **2016**, *120*, 7482–7490. [[CrossRef](#)]

60. Wang, J.; Zhang, L.; Fang, W.; Ren, J.; Li, Y.; Yao, H.; Wang, J.; Li, Z. Enhanced Photoreduction CO₂ Activity over Direct Z-Scheme α -Fe₂O₃/Cu₂O Heterostructures under Visible Light Irradiation. *ACS Appl. Mater. Interfaces* **2015**, *7*, 8631–8639. [[CrossRef](#)]
61. Newbury, D.E.; Ritchie, N.W.M. Is Scanning Electron Microscopy/Energy Dispersive X-ray Spectrometry (SEM/EDS) Quantitative? *Scanning* **2013**, *35*, 141–168. [[CrossRef](#)]
62. Parish, C.M.; Brewer, L.N. Key Parameters Affecting Quantitative Analysis of STEM-EDS Spectrum Images. *Microsc. Microanal.* **2010**, *16*, 259–272. [[CrossRef](#)]
63. Morrison, C.; Sun, H.; Yao, Y.; Loomis, R.A.; Buhro, W.E. Methods for the ICP-OES Analysis of Semiconductor Materials. *Chem. Mater.* **2020**, *32*, 1760–1768. [[CrossRef](#)]
64. Li, C.; Yan, N.; Ye, Y.; Lv, Z.; He, X.; Huang, J.; Zhang, N. Thermal analysis and stability of boron/potassium nitrate pyrotechnic composition at 180 °C. *Appl. Sci.* **2019**, *9*, 3630. [[CrossRef](#)]
65. Bykova, E.; Dubrovinsky, L.; Dubrovinskaia, N.; Bykov, M.; McCammon, C.; Ovsyannikov, S.V.; Liermann, H.P.; Kuppenko, I.; Chumakov, A.I.; Rüffer, R.; et al. Structural Complexity of Simple Fe₂O₃ at High Pressures and Temperatures. *Nat. Commun.* **2016**, *7*, 1–6. [[CrossRef](#)] [[PubMed](#)]